

1**Evaluation of autoconversion and accretion enhancement factors in GCM warm-rain**  
2**parameterizations using ground-based measurements at the Azores**

3Peng Wu<sup>1</sup>, \*Baiké Xi<sup>1</sup>, Xiquan Dong<sup>1</sup>, and Zhibo Zhang<sup>2</sup>

4<sup>1</sup> Department of Hydrology and Atmospheric Sciences, The University of Arizona, Tucson,  
5Arizona, USA

6<sup>2</sup> Physics Department, The University of Maryland, Baltimore County, Maryland, USA

7

8

9 Submitted to Atmospheric Chemistry and Physics (August 17, 2018)

10

11

12**Keywords:** MBL clouds, enhancement factors, autoconversion and accretion parameterizations

13

14

15

16

17

18\* Corresponding author address: Dr. Baiké Xi, Department of Hydrology and Atmospheric  
19Sciences, University of Arizona, 1133 E. James E. Rogers Way, Tucson, AZ 85721-0011.  
20baikexi@email.arizona.edu; Phone: 520-626-8945

21 **Abstract**

22 A great challenge in climate modelling is how to parametrize sub-grid cloud processes, such  
23 as autoconversion and accretion in warm rain formation. In this study, we use ground-based  
24 observations and retrievals over the Azores to investigate the so-called enhancement factors,  
25  $E_{auto}$  and  $E_{accr}$ , which are often used in climate models to account for the influences of sub-grid  
26 variances of cloud and precipitation water on the autoconversion and accretion processes.  $E_{auto}$   
27 and  $E_{accr}$  are computed for different model resolutions. The calculated  $E_{auto}$  values increase  
28 from 1.96 (30 km) to 3.15 (120 km), and the calculated  $E_{accr}$  values increase from 1.53 (30 km)  
29 to 1.76 (180 km). Comparing the prescribed enhancement factors in Morrison and Gettleman  
30 (2008, MG08) to the observed ones, we found that a higher  $E_{auto}$  (3.2) at small grids and lower  
31  $E_{accr}$  (1.07) are used in MG08, which helps to explain why most of the GCMs produce too  
32 frequent precipitation events but with too light precipitation intensity. The ratios of rain to  
33 cloud water mixing ratio at  $E_{accr}=1.07$  and  $E_{accr}=2.0$  are 0.063 and 0.142, respectively, further  
34 proving that the prescribed value of  $E_{accr}=1.07$  used in MG08 is too small to simulate correct  
35 precipitation intensity. Both  $E_{auto}$  and  $E_{accr}$  increase when the boundary layer becomes less  
36 stable, and the values are larger in precipitating clouds ( $CLWP > 75 \text{ gm}^{-2}$ ) than those in  
37 nonprecipitating clouds ( $CLWP < 75 \text{ gm}^{-2}$ ). Therefore, the selection of  $E_{auto}$  and  $E_{accr}$  values in  
38 GCMs should be regime-dependent.

39

## 40 **1. Introduction**

41 Due to their vast areal coverage (Warren et al., 1986, 1988; Hahn and Warren, 2007) and  
42 strong radiative cooling effect (Hartmann et al., 1992; Chen et al., 2000), small changes in the  
43 coverage or thickness of marine boundary layer (MBL) clouds could change the radiative  
44 energy budget significantly (Hartmann and Short, 1980; Randall et al., 1984) or even offset the  
45 radiative effects produced by increasing greenhouse gases (Slingo, 1990). The lifetime of MBL  
46 clouds remains an issue in climate models (Yoo and Li, 2012; Jiang et al., 2012; Yoo et al.,  
47 2013; Stanfield et al., 2014) and represents one of the largest uncertainties in predicting future  
48 climate (Wielicki et al., 1995; Houghton et al., 2001; Bony and Dufresne, 2005).

49 MBL clouds frequently produce precipitation, mostly in the form of drizzle (Austin et al.,  
50 1995; Wood, 2005a; Leon et al., 2008; Wood, 2012). A significant amount of drizzle is  
51 evaporated before reaching the surface, for example, about ~76% over the Azores region in  
52 Northeast Atlantic (Wu et al., 2015), which provides another water vapour source for MBL  
53 clouds. Due to their pristine environment and their close vicinity to the surface, MBL clouds  
54 are especially sensitive to aerosol perturbations (Quaas et al., 2009; Kooperman et al., 2012).  
55 Most aerosol indirect effects are associated with precipitation suppression (Albrecht, 1989;  
56 Ackerman et al., 2004; Lohmann and Feichter, 2005; Wood, 2007). Thus, accurate prediction  
57 of precipitation is essential in simulating the global energy budget and in constraining aerosol  
58 indirect effects in climate projections.

59 Due to the coarse spatial resolutions of the general circulation model (GCM) grid, many  
60 cloud processes cannot be adequately resolved and must be parameterized. For example, warm  
61 rain parameterizations in most GCMs treat the condensed water as either cloud or rain from the  
62 collision-coalescence process, which is partitioned into autoconversion and accretion sub-  
63 processes in model parameterizations (Kessler, 1969; Tripoli and Cotton, 1980; Beheng, 1994;  
64 Khairoutdinov and Kogan, 2000; Liu and Daum, 2004). Autoconversion represents the process  
65 that drizzle drops being formed through the condensation of cloud droplets and accretion  
66 represents the process where rain drops grow by the coalescence of drizzle-sized drops with  
67 cloud droplets. Autoconversion mainly accounts for precipitation initiation while accretion  
68 primarily contributes to precipitation intensity. Autoconversion is often parameterized as  
69 functions of cloud droplet number concentration ( $N_c$ ) and cloud water mixing ratio ( $q_c$ ), while  
70 accretion depends on both cloud and rain water mixing ratios ( $q_c$  and  $q_r$ ) (Kessler, 1969; Tripoli  
71 and Cotton, 1980; Beheng, 1994; Khairoutdinov and Kogan, 2000; Liu and Daum, 2004;  
72 Wood, 2005b). All previous studies suggested that these two processes as power law functions  
73 of cloud and precipitation properties (See section 2 for details).

74 In conventional GCMs, the lack of information on the sub-grid variances of cloud and  
75 precipitation leads to the unavoidable use of the grid-mean quantities ( $\overline{N_c}$ ,  $\overline{q_c}$ , and  $\overline{q_r}$ , where  
76 overbar denotes grid mean, same below) in calculating autoconversion and accretion rates.  
77 MBL cloud liquid water path (CLWP) distributions are often positive skewed (Wood and

78 Hartmann, 2006; Dong et al., 2014a and 2014b), that is, the mean value is greater than mode  
79 value. Thus, the mean value only represents a relatively small portion of samples. Also, due to  
80 the nonlinear nature of the relationships, the two processes depend significantly on the sub-  
81 grid variability and co-variability of cloud and precipitation microphysical properties (Weber  
82 and Quass, 2012; Boutle et al., 2014). In some GCMs, sub-grid scale variability is often ignored  
83 or hard coded using constants to represent the variabilities under all meteorological conditions  
84 and across the entire globe (Pincus and Klein, 2000; Morrison and Gettleman, 2008; Lebsock  
85 et al., 2013). This could lead to systematic errors in precipitation rate simulations (Wood et al.,  
86 2002; Larson et al., 2011; Lebsock et al., 2013; Boutle et al., 2014; Song et al., 2018), where  
87 GCMs are found to produce too frequent but too light precipitation compared to observations  
88 (Zhang et al., 2002; Jess, 2010; Stephens et al., 2010; Nam and Quaas, 2012; Song et al., 2018).  
89 The bias is found to be smaller by using a probability density function (PDF) of cloud water to  
90 represent the sub-grid scale variability in autoconversion parameterization (Beheng, 1994;  
91 Zhang et al., 2002; Jess, 2010), or more complexly, by integrating the autoconversion rate over  
92 a joint PDF of liquid water potential temperature, vertical velocity, total water mixing ratio and  
93 rain water mixing ratio (Cheng and Xu, 2009).

94 Process rate enhancement factors ( $E$ ) are introduced when considering sub-grid scale  
95 variability in parameterizing grid-mean processes and they should be parameterized as  
96 functions of the PDFs of cloud and precipitation properties within a grid box (Morrison and

97 Gettleman, 2008; Lebsock et al., 2013; Boutle et al., 2014). However, these values in some  
98 GCM parameterization schemes are prescribed as constants regardless of underlying surface  
99 or meteorological conditions (Xie and Zhang, 2015). Boutle et al. (2014) used aircraft in situ  
100 measurements and remote sensing techniques to develop a parameterization for cloud and rain,  
101 in which not only consider the sub-grid variabilities under different grid scales, but also  
102 consider the variation of cloud and rain fractions. The parameterization was found to reduce  
103 precipitation estimation bias significantly. Hill et al. (2015) modified this parameterization and  
104 developed a regime and cloud type dependent sub-grid parameterization, which was  
105 implemented to the Met Office Unified Model by Walters et al. (2017) and found that the  
106 radiation bias is reduced using the modified parameterization. Using ground-based  
107 observations and retrievals, Xie and Zhang (2015) proposed a scale-aware cloud  
108 inhomogeneity parameterization that they applied to the Community Earth System Model  
109 (CESM) and found that it can recognize spatial scales without manual tuning. The  
110 inhomogeneity parameter is essential in calculating enhancement factors and affect the  
111 conversion rate from cloud to rain liquid. Xie and Zhang (2015), however, did not evaluate the  
112 validity of CESM simulations from their parameterization; the effect of  $N_c$  variability or the  
113 effect of covariance of cloud and rain on accretion process was not assessed. Most recently,  
114 Zhang et al. (2018) derived the sub-grid CLWP and  $N_c$  from the MODIS cloud product. They  
115 also studied the implication of the sub-grid cloud property variations for the autoconversion

116 rate simulation, in particular the enhancement factor, in GCMs. For the first time, the  
117 enhancement factor due to the sub-grid variation of  $N_c$  is derived from satellite observation,  
118 and results reveal several regions downwind of biomass burning aerosols (e.g., Gulf of Guinea,  
119 East Coast of South Africa), air pollution (i.e., Eastern China Sea), and active volcanos (e.g.,  
120 Kilauea Hawaii and Ambae Vanuatu), where the enhancement factor due to  $N_c$  is comparable,  
121 or even larger than that due to CLWP. However, one limitation of Zhang et al. (2018) is the  
122 use of passive remote sensing data only, which cannot distinguish cloud and rain water.

123 Dong et al. (2014a and 2014b) and Wu et al. (2015) reported MBL cloud and rain properties  
124 over the Azores and provided the possibility of calculating the enhancement factors using  
125 ground-based observations and retrievals. A joint retrieval method to estimate  $q_c$  and  $q_r$  profiles  
126 is proposed based on existing studies and is presented in Appendix A. Most of the calculations  
127 and analyses in this study is based on Morrison and Gettleman (2008, MG08 hereafter) scheme.  
128 The enhancement factors in several other schemes are also discussed and compared with the  
129 observational results and the approach in this study can be repeated for other microphysics  
130 schemes in GCMs. This manuscript is organized as follows: section 2 includes a summary of  
131 the mathematical formulas from previous studies that can be used to calculate grid-mean  
132 process enhancement factors. Ground-based observations and retrievals are introduced in  
133 Section 3. Section 4 presents results and discussions, followed by summary and conclusions in  
134 Section 5. The retrieval method used in this study is in Appendix A.

## 135 2. Mathematical Background

136 Autoconversion and accretion rates in GCMs are usually parameterized as power law  
137 equations (Tripoli and Cotton, 1980; Beheng, 1994; Khairoutdinov and Kogan, 2000; Liu and  
138 Daum, 2004):

$$139 \left( \frac{\partial q_r}{\partial t} \right)_{auto} = A \bar{q}_c^{a1} \bar{N}_c^{a2}, \quad (1)$$

$$140 \left( \frac{\partial q_r}{\partial t} \right)_{accr} = B (\bar{q}_c \bar{q}_r)^b, \quad (2)$$

141 where  $A$ ,  $a1$ ,  $a2$ ,  $B$ , and  $b$  are coefficients in different schemes listed in Table 1. The  $\bar{q}_c$ ,  $\bar{q}_r$ ,  
142 and  $\bar{N}_c$  are grid-mean cloud water mixing ratio, rain water mixing ratio, and droplet number  
143 concentration, respectively. Because it is widely used in model parameterizations, the detailed  
144 results from Khairoutdinov and Kogan (2000) parameterization that been used in MG08  
145 scheme will be shown in Section 4 while a summary will be given for other schemes.

146 Ideally, the covariance between physical quantities should be considered in the calculation  
147 of both processes. However,  $\bar{q}_c$  and  $\bar{N}_c$  in Eq. (1) are arguably not independently retrieved in  
148 our retrieval method which will be introduced in this section and Appendix A. Thus we only  
149 assess the individual roles of  $q_c$  and  $N_c$  sub-grid variations in determining autoconversion rate.  
150  $q_c$  and  $q_r$ , on the other hand, are retrieved from two independent algorithms as shown in Dong  
151 et al. (2014a and 2014b), Wu et al. (2015) and Appendix A, we will assess the effect of cloud  
152 and rain property covariance on accretion rate calculations.

153 In the sub-grid scale, the PDFs of  $q_c$  and  $N_c$  are assumed to follow a gamma distribution  
 154 based on observational studies of optical depth in MBL clouds (Barker et al., 1996; Pincus et  
 155 al., 1999; Wood and Hartmann, 2006):

$$156 \quad P(x) = \frac{\alpha^\nu}{\Gamma(\nu)} x^{\nu-1} e^{-\alpha x}, \quad (3)$$

157 where  $x$  represents  $q_c$  or  $N_c$  with grid-mean quantity  $\bar{q}_c$  or  $\bar{N}_c$ , represented by  $\mu$ ,  $\alpha = \nu/\mu$  is the  
 158 scale parameter,  $\sigma^2$  is the relative variance of  $x$  (= variance divided by  $\mu^2$ ),  $\nu = 1/\sigma^2$  is the  
 159 shape parameter.  $\nu$  is an indicator of cloud field homogeneity, with large values representing  
 160 homogeneous and small values indicating inhomogeneous cloud field.

161 By integrating autoconversion rate, Eq. (1), over the grid-mean rate, Eq. (3), with respect  
 162 to sub-grid scale variation of  $q_c$  and  $N_c$ , the autoconversion rate can be expressed as:

$$163 \quad \left(\frac{\partial q_r}{\partial t}\right)_{auto} = A \mu_{q_c}^{a1} \mu_{N_c}^{a2} \frac{\Gamma(\nu+a)}{\Gamma(\nu)\nu^a}, \quad (4)$$

164 where  $a = a1$  or  $a2$ . Comparing Eq. (4) to Eq. (1), the autoconversion enhancement factor  
 165 ( $E_{auto}$ ) can be given with respect to  $q_c$  and  $N_c$ :

$$166 \quad E_{auto} = \frac{\Gamma(\nu+a)}{\Gamma(\nu)\nu^a}. \quad (5)$$

167 In addition to fitting the distributions of  $q_c$  and  $N_c$ , we also tried two other methods to  
 168 calculate  $E_{auto}$ . The first is to integrate Eq. (1) over the actual PDFs from observed or retrieved  
 169 parameters and the second is to fit a lognormal distribution for sub-grid variability like what  
 170 has been done in other studies (e.g., Lebsock et al., 2013; Larson and Griffin, 2013). It is found

171 that all three methods get similar results. In this study, we use a gamma distribution that is  
 172 consistent with MG08. Also note that, in the calculation of  $E_{auto}$  from  $\overline{N}_c$ , the negative exponent  
 173 (-1.79) may cause singularity problems in Eq. (5). When this situation occurs, we do direct  
 174 calculations by integrating the PDF of  $\overline{N}_c$  rather than using Eq. (5).

175 To account for the covariance of microphysical quantities in a model grid, it is difficult to  
 176 apply bivariate gamma distribution due to its complex nature. In this study, the bivariate  
 177 lognormal distribution of  $q_c$  and  $q_r$  is used (Lebsock et al., 2013; Boutle et al., 2014) and can  
 178 be written as:

$$\begin{aligned}
 179 \quad P(\overline{q}_c, \overline{q}_r) &= \frac{1}{2\pi\overline{q}_c\overline{q}_r\sigma_{q_c}\sigma_{q_r}\sqrt{1-\rho^2}} \exp\left\{-\frac{1}{2}\frac{1}{1-\rho^2}\left[\left(\frac{\ln\overline{q}_c-\mu_{q_c}}{\sigma_{q_c}}\right)^2 - 2\rho\left(\frac{\ln\overline{q}_c-\mu_{q_c}}{\sigma_{q_c}}\right)\left(\frac{\ln\overline{q}_r-\mu_{q_r}}{\sigma_{q_r}}\right) + \right. \right. \\
 180 \quad &\left.\left.\left(\frac{\ln\overline{q}_r-\mu_{q_r}}{\sigma_{q_r}}\right)^2\right]\right\}, \tag{6}
 \end{aligned}$$

181 where  $\sigma$  is standard deviation and  $\rho$  is the correlation coefficient of  $q_c$  and  $q_r$ .

182 Similarly, by integrating the accretion rate in Eq. (2) from Eq. (6), we get the accretion  
 183 enhancement factor ( $E_{accr}$ ) of:

$$184 \quad E_{accr} = \left(1 + \frac{1}{v_{q_c}}\right)^{\frac{1.15^2-1.15}{2}} \left(1 + \frac{1}{v_{q_r}}\right)^{\frac{1.15^2-1.15}{2}} \exp(\rho 1.15^2 \sqrt{\ln\left(1 + \frac{1}{v_{q_c}}\right) \ln\left(1 + \frac{1}{v_{q_r}}\right)}). \tag{7}$$

### 185 3. Ground-based observations and retrievals

186 The datasets used in this study were collected at the Department of Energy (DOE)  
187 Atmospheric Radiation Measurement (ARM) Mobile Facility (AMF), which was deployed on  
188 the northern coast of Graciosa Island (39.09°N, 28.03°W) from June 2009 to December 2010  
189 (for more details, please refer to Rémillard et al., 2012; Dong et al., 2014a and Wood et al.,  
190 2015). The detailed operational status of the remote sensing instruments on AMF was  
191 summarized in Figure 1 of Rémillard et al. (2012) and discussed in Wood et al. (2015). The  
192 ARM Eastern North Atlantic (ENA) site was established on the same island in 2013 and  
193 provides long-term continuous observations.

194 The cloud-top heights ( $Z_{top}$ ) were determined from W-band ARM cloud radar (WACR)  
195 reflectivity and only single-layered low-level clouds with  $Z_{top} \leq 3$  km are selected. Cloud-base  
196 heights ( $Z_{base}$ ) were detected by a laser ceilometer (CEIL) and the cloud thickness was simply  
197 the difference between cloud top and base heights. The cloud liquid water path (CLWP) was  
198 retrieved from microwave radiometer (MWR) brightness temperatures measured at 23.8 and  
199 31.4 GHz using a statistical retrieval method with an uncertainty of  $20 \text{ g m}^{-2}$  for  $CLWP < 200$   
200  $\text{g m}^{-2}$ , and 10% for  $CLWP > 200 \text{ g m}^{-2}$  (Liljegren et al., 2001; Dong et al., 2000). Precipitating  
201 status is identified through a combination of WACR reflectivity and  $Z_{base}$ . As in Wu et al.  
202 (2015), we labelled the status of a specific time as “precipitating” if the WACR reflectivity  
203 below the cloud base exceeds -37 dBZ.

204 The ARM merged sounding data have a 1-min temporal and 20-m vertical resolution below  
205 3 km (Trojan, 2012). In this study, the merged sounding profiles are averaged to 5-min  
206 resolution. Pressure and temperature profiles are used to calculate air density ( $\rho_{air}$ ) profiles  
207 and to infer adiabatic cloud water content.

208 Cloud droplet number concentration ( $N_c$ ) is retrieved using the methods presented in Dong  
209 et al. (1998, 2014a and 2014b) and are assumed to be constant in a cloud layer. Vertical profiles  
210 of cloud and rain water content (CLWC and RLWC) are retrieved by combining WACR  
211 reflectivity, CEIL attenuated backscatter and by assuming adiabatic growth of cloud parcels.  
212 The detailed description is presented in Appendix A with the results from a selected case. The  
213 CLWC and RLWC values are transformed to  $q_c$  and  $q_r$  by dividing by air density (e.g.,  $q_c(z) =$   
214  $CLWC(z)/\rho_{air}(z)$ ).

215 The estimated uncertainties for the retrieved  $q_c$  and  $q_r$  are 30% and 18%, respectively (see  
216 Appendix A). We used the estimated uncertainties of  $q_r$  and  $q_c$  as inputs of Eqs. (4) and (7) to  
217 assess the uncertainties of  $E_{auto}$  and  $E_{accr}$ . For instance,  $(1 \pm 0.3)q_c$  are used in Eq. (4) and the  
218 mean differences are then used as the uncertainty of  $E_{auto}$ . Same method is used to estimate the  
219 uncertainty for  $E_{accr}$ .

220 The autoconversion and accretion parameterizations partitioned from the collision-  
221 coalescence process dominate at different levels in a cloud layer. Autoconversion dominates  
222 around cloud top where cloud droplets reach maximum by condensation and accretion is

223 dominant at middle and lower parts of the cloud where rain drops sediment and continue to  
224 grow by collecting cloud droplets. Complying with the physical processes, we estimate  
225 autoconversion and accretion rates at different levels of a cloud layer in this study. The  
226 averaged  $q_c$  within the top five range gates (~215 m thick) are used to calculate  $E_{auto}$ . To  
227 calculate  $E_{accr}$ , we use the averaged  $q_c$  and  $q_r$  within five range gates around the maximum  
228 radar reflectivity. If the maximum radar reflectivity appears at the cloud base, then five range  
229 gates above the cloud base are used.

230 The ARM merged sounding data are also used to calculate lower tropospheric stability  
231 (LTS), which is used to infer the boundary layer stability. In this study, unstable and stable  
232 boundary layers are defined as LTS less than 13.5 K and greater than 18 K, respectively, and  
233 environment with an LTS between 13.5 K and 18 K is defined as mid-stable (Wang et al. 2012;  
234 Bai et al. 2018). Enhancement factors in different boundary layers are summarized in Section  
235 4.2 and may be used as references for model simulations. Further, two regimes are classified:  
236 CLWP greater than  $75 \text{ g m}^{-2}$  as precipitating and CLWP less than  $75 \text{ g m}^{-2}$  as nonprecipitating  
237 (Rémillard et al., 2012).

238 To evaluate the dependence of autoconversion and accretion rates on sub-grid variabilities  
239 for different model spatial resolutions, an averaged wind speed within a cloud layer was  
240 extracted from merged sounding and used in sampling observations over certain periods to  
241 mimic different grid sizes in GCMs. For example, two hours of observations corresponds to a

242 72-km grid box if mean in-cloud wind speed is  $10 \text{ m s}^{-1}$  horizontal wind and if the wind speed  
243 is  $5 \text{ m s}^{-1}$ , four hours of observations is needed to mimic the same grid. We used six grid sizes  
244 (30-, 60-, 90-, 120-, 150-, and 180-km) and mainly show the results from 60-km and 180-km  
245 grid sizes in Section 4.

## 246 **4. Results and discussions**

247 In this section, we first show the data and methods using a selected case, followed by  
248 statistical analysis based on 19-month of data and multiple time-intervals.

### 249 **4.1 Case study**

250 The selected case occurred on July 27, 2010 (Figure 1a) at the Azores. This case was  
251 characterized by a long time of non-precipitating or light drizzling cloud development (00:00-  
252 14:00 UTC) before intense drizzling occurred (14:00-20:00 UTC). Wu et al. (2017) studied  
253 this case in detail to demonstrate the effect of wind shear on drizzle initiation. Here, we choose  
254 two periods corresponding to a 180-km grid and having similar mean  $q_c$  near cloud top:  $0.28 \text{ g}$   
255  $\text{kg}^{-1}$  for period c and  $0.26 \text{ g kg}^{-1}$  for period d but with different distributions (Figures 1c and  
256 1d). The PDFs of  $q_c$  are then fitted using gamma distributions to get shape parameters ( $\nu$ ) as  
257 shown in Figures 1c and 1d. Smaller  $\nu$  is usually associated with more inhomogeneous cloud  
258 field, which allows more rapid drizzle production and more efficient liquid transformation from  
259 cloud to rain (Xie and Zhang, 2015) in regions that satisfy precipitation criteria, which is  
260 usually controlled using threshold  $q_r$ , droplet size or relative humidity (Kessler, 1969; Liu and

261 Daum, 2004). The period d has a wider  $q_c$  distribution than the period c, resulting in a smaller  
262  $\nu$  and thus larger  $E_{auto}$ . Using the fitted  $\nu$ , the  $E_{auto}$  from  $q_c$  is calculated from Eq. (5) and the  
263 period d is larger than the period c (1.80 vs. 1.33). The  $E_{auto}$  values for the periods d and c can  
264 also be calculated from  $N_c$  using the same procedure as  $q_c$  with similar result (2.1 vs. 1.51). The  
265  $E_{accr}$  values for the periods d and c can be calculated from the covariance of  $q_c$  and  $q_r$  and Eq.  
266 (7). Not surprisingly, the period d has larger  $E_{accr}$  than the period c. The combination of larger  
267  $E_{auto}$  and  $E_{accr}$  in the period d contributes to the rapid drizzle production and high rain rate as  
268 seen from WACR reflectivity and  $q_r$ .

269 It is important to understand the physical meaning of enhancement factors in precipitation  
270 parameterization. For example, if we assume two scenarios for  $q_c$  with a model grid having the  
271 same mean values but different distributions: (1) The distribution is extremely homogeneous,  
272 there will be no sub-grid variability because the cloud has the same chance to precipitate and  
273 the enhancement factors would be unity (this is true for arbitrary grid-mean  $q_c$  amount as well).  
274 (2) The cloud field gets more and more inhomogeneous with a broad range of  $q_c$  within the  
275 model grid box, which results in a greater enhancement factor and increases the possibility of  
276 precipitation. That is, a large enhancement factor can make the part of cloud with higher  $q_c$   
277 within the grid box become more efficient in generating precipitation, rather than the entire  
278 model grid.

279 It is clear that  $q_c$  and  $N_c$  in Figure 1b are correlated with each other. In addition to their  
280 natural relationships,  $q_c$  and  $N_c$  in our retrieval method are also correlated (Dong et al., 2014a  
281 and 2014b). Thus, the effect of  $q_c$  and  $N_c$  covariance on  $E_{auto}$  is not included in this study. In  
282 Figures 1c and 1d, the results are calculated using model grid of 180-km for the selected case  
283 on 27 July 2010. In Section 4.2, we will use these approaches to calculate their statistical results  
284 for multiple grid sizes using the 19-month ARM ground-based observations and retrievals.

## 285 **4.2 Statistical result**

286 For a specific grid size, e.g. 60-km, we estimate the shape parameter ( $\nu$ ) and calculate  $E_{auto}$   
287 through Eqns. (5) and (7). The PDFs of  $E_{auto}$  for both 60-km and 180-km grids are shown in  
288 Figures 2a-2d. The distributions of  $E_{auto}$  values calculated from  $q_c$  with 60-km and 180-km grid  
289 sizes (Figures 2a and 2b) are different to each other (2.79 vs. 3.3). The calculated  $E_{auto}$  values  
290 range from 1 to 10, and most are less than 4. The average value for the 60-km grid (2.79) is  
291 smaller than that for the 180-km grid (3.2), indicating a possible dependence of  $E_{auto}$  on model  
292 grid size. Because drizzle-sized drops are primarily resulted from autoconversion, we  
293 investigate the relationship between  $E_{auto}$  and precipitation frequency, which is defined as the  
294 average percentage of drizzling occurrence based on radar reflectivity below the cloud base.  
295 The precipitation frequency (black lines in Figures 2a and 2b) within each PDF bin shows an  
296 increasing trend for  $E_{auto}$  from 0 to 4-6, then oscillates around a relative constant when  $E_{auto} >$   
297 6, indicating that in precipitation initiation process,  $E_{auto}$  keeps increasing to a certain value

298 (~6) until the precipitation frequency reaches a near-steady state. Larger  $E_{auto}$  values do not  
299 necessarily result in higher precipitation frequency but instead may produce more drizzle-sized  
300 drops from autoconversion process when the cloud is precipitating. Therefore, the  $E_{auto}$  value  
301 of 6 is a critical threshold for converting cloud droplets into rain drops within MBL clouds in  
302 MG08.

303 The PDFs of  $E_{auto}$  calculated from  $N_c$  also share similar patterns of positive skewness and  
304 peaks at ~1.5-2.0 for the 60-km and 180-km grid sizes (Figures 2c and 2d). Although the  
305 average values are close to their  $q_c$  counterparts (2.54 vs. 2.79 for 60-km and 3.45 vs. 3.2 for  
306 180-km), the difference in  $E_{auto}$  between 60-km and 180-km grid sizes becomes large. The  
307 precipitation frequencies within each bin are nearly constant or slightly decrease, which are  
308 different to their  $q_c$  counterparts shown in Figures 2a and 2b. This suggests complicated effects  
309 of droplet number concentration on precipitation initiation and warrants more explorations of  
310 aerosol-cloud-precipitation interactions. This is very intriguing result, which suggests the  
311 existence of significant sub-grid variation of  $N_c$  and this variation can significantly influence  
312 the warm rain process. As mentioned in Section 2,  $q_c$  and  $N_c$  are also fitted using lognormal  
313 distributions to calculate  $E_{auto}$ , those are close to the results in Figure 2 (not shown here) with  
314 average values of 3.28 and 3.84, respectively, for 60-km and 180-km grid sizes. Because the  
315  $E_{auto}$  values calculated from  $q_c$  and  $N_c$  are close to each other, we will focus on analyzing the  
316 results from  $q_c$  only for simplicity and clarity. The effect of  $q_c$  and  $N_c$  covariance, as stated in

317 Section 4.1, is not presented in this study due to the intrinsic correlation in the retrieval (Dong  
318 et al., 2014a and 2014b and Appendix A of this study).

319 The covariance of  $q_c$  and  $q_r$  is included in calculating  $E_{accr}$  and the results are shown in  
320 Figures 2e and 2f. The calculated  $E_{accr}$  values range from 1 to 4 with mean values of 1.62 and  
321 1.76 for 60-km and 180-km grid sizes, respectively. These two mean values are much greater  
322 than the prescribed value used in MG08 (1.07). Since accretion is dominant at middle and lower  
323 parts of the cloud where rain drops sediment and continue to grow by collecting cloud droplets,  
324 we superimpose the ratio of  $q_r$  to  $q_c$  within each bin (black lines in Figures 2e and 2f) to  
325 represent the portion of rain water in the cloud layer. In both panels, the ratios are less than  
326 15%, which means that  $q_r$  can be one order of magnitude smaller than  $q_c$ . The differences in  
327 magnitude are consistent with previous CloudSat and aircraft results (e.g., Boutle et al., 2014).  
328 This ratio increases from  $E_{accr}=0$  to  $\sim 2$ , and then decreases, suggesting a possible optimal state  
329 for the collision-coalescence process to achieve maximum efficiency for converting cloud  
330 water into rain water at  $E_{accr}=2$ . In other words, the conversion efficiency cannot be infinitely  
331 increased with  $E_{accr}$  under available cloud water. The ratios of  $q_r$  to  $q_c$  at  $E_{accr}=1.07$  and  
332  $E_{accr}=2.0$  are 0.063 and 0.142, respectively, further proving that the prescribed value of  
333  $E_{accr}=1.07$  used in MG08 is too small to simulate correct precipitation intensity in the models.  
334 Therefore, similar to the conclusions in Lebsock et al. (2013) and Boutle et al. (2014), we  
335 suggest increasing  $E_{accr}$  from 1.07 to 1.5-2.0 in GCMs.

336 To illustrate the impact of using prescribed enhancement factors, autoconversion and  
337 accretion rates are calculated using the prescribed values (e.g., 3.2 for  $E_{auto}$  and 1.07 for  $E_{accr}$ ,  
338 MG08; Xie and Zhang, 2015) and the newly calculated ones in Figure 2 that use observations  
339 and retrievals. Figure 3 shows the joint density of autoconversion (Figures 3a and 3b) and  
340 accretion rates (Figures 3c and 3d) from observations (x-axis) and model parameterizations (y-  
341 axis) for 60-km and 180-km grid sizes. Despite the spread, the peaks of the joint density of  
342 autoconversion rate appear slightly above the one-to-one line, suggesting that cloud droplets in  
343 the model are more easily to be converted into drizzle/rain drops than observations. On the  
344 other hand, the peaks of accretion rate appear slightly below the one-to-one line which indicates  
345 that simulated precipitation intensities are lower than observed ones. The magnitudes of the  
346 two rates are consistent with Khairoutdinov and Kogan (2000), Liu and Daum (2004), and  
347 Wood (2005b).

348 Compared to the observations, the precipitation in GCMs occurs at higher frequencies with  
349 lower intensities, which might explain why the total precipitation amounts are close to surface  
350 measurements over an entire grid box. This ‘promising’ result, however, fails to simulate  
351 precipitation on the right scale and cannot capture the correct rain water amount, thus providing  
352 limited information in estimating rain water evaporation and air-sea energy exchange.

353 Clouds in an unstable boundary layer have a better chance of getting moisture supply from  
354 the surface by upward motion than clouds in a stable boundary layer. Precipitation frequencies

355 are thus different in these two boundary layer regimes. For example, clouds in a relatively  
356 unstable boundary layer seem easier to produce drizzle than those in a stable boundary layer  
357 (Wu et al., 2017). Provided the same boundary layer condition, CLWP is an important factor  
358 in determining the precipitation status of clouds. At the Azores, precipitating clouds are more  
359 likely to have CLWP greater than  $75 \text{ g m}^{-2}$  than their nonprecipitating counterparts (Rémillard  
360 et al., 2012). To further investigate what conditions and parameters can significantly influence  
361 the enhancement factors, we classify low-level clouds according to their boundary layer  
362 conditions and CLWPs.

363 The averaged  $E_{auto}$  and  $E_{accr}$  values for each category are listed in Table 2. Both  $E_{auto}$  and  
364  $E_{accr}$  increase when the boundary layer becomes less stable, and these values become larger in  
365 precipitating clouds ( $\text{CLWP} > 75 \text{ gm}^{-2}$ ) than those in nonprecipitating clouds ( $\text{CLWP} < 75 \text{ gm}^{-2}$ ).  
366 In real applications, autoconversion process only occurs when  $q_c$  or cloud droplet size reaches  
367 a certain threshold (e.g., Kessler, 1969 and Liu and Daum, 2004). Thus, it will not affect model  
368 simulations if a valid  $E_{auto}$  is assigned to Eq. (1) in a nonprecipitating cloud. The  $E_{auto}$  values  
369 in both stable and mid-stable boundary layer conditions are smaller than the prescribed value  
370 of 3.2, while the values in unstable boundary layers are significantly larger than 3.2 regardless  
371 of if they are precipitating or not. All  $E_{accr}$  values are greater than the constant of 1.07. The  
372  $E_{auto}$  values in Table 2 range from 2.32 to 6.94 and the  $E_{accr}$  values vary from 1.42 to 1.86,

373 depending on different boundary layer conditions and CLWPs. Therefore, as suggested by Hill  
374 et al. (2015), the selection of  $E_{auto}$  and  $E_{accr}$  values in GCMs should be regime-dependent.

375 To properly parameterize sub-grid variabilities, the approaches by Hill et al. (2015) and  
376 Walters et al. (2017) can be adopted. To use MG08 and other parameterizations in GCMs as  
377 listed in Table 1, proper adjustments can be made according to the model grid size, boundary  
378 layer conditions, and precipitating status. As stated in the methodology, we used a variety of  
379 model grid sizes. Figure 4 demonstrates the dependence of both enhancement factors on  
380 different model grid sizes. The  $E_{auto}$  values (red line) increase from 1.97 at a grid box of 30×30  
381 km to 3.15 at a grid box of 120×120 km, which are 38.4% and 2% percent lower than the  
382 prescribed value (3.2, upper dashed line). After that, the  $E_{auto}$  values remain relatively constant  
383 of ~3.18 when the model grid is 180 km, which is close to the prescribed value of 3.2 used in  
384 MG08. This result indicates that the prescribed value in MG08 represents well in large grid  
385 sizes in GCMs. The  $E_{accr}$  values (blue line) increase from 1.53 at a grid box of 30×30 km to  
386 1.76 at a grid box of 180×180 km, those are 43% and 64%, respectively, larger than the  
387 prescribed value (1.07, lower dashed line). The shaded areas represent the uncertainties of  $E_{auto}$   
388 and  $E_{accr}$  associated with the uncertainties of the retrieved  $q_c$  and  $q_r$ . When model grid size  
389 increases, the uncertainties slightly decrease. The prescribed  $E_{auto}$  is close to the upper  
390 boundary of uncertainties except for the 30-km grid size, while the prescribed  $E_{accr}$  is  
391 significantly lower than the lower boundary.

392 It is noted that  $E_{auto}$  and  $E_{accr}$  depart from their prescribed values at opposite directions as  
393 model grid size increases. For models with finer resolutions (e.g., 30-km), both  $E_{auto}$  and  $E_{accr}$   
394 are significantly different from the prescribed values, which can partially explain the issue of  
395 ‘too frequent’ and ‘too light’ precipitation. Under both conditions, the accuracy of precipitation  
396 estimation is degraded. For models with coarser resolutions (e.g., 180-km), average  $E_{auto}$  is  
397 exactly 3.2 while  $E_{accr}$  is much larger than 1.07 when compared to finer resolution simulations.  
398 In such situations, the simulated precipitation will be dominated by the ‘too light’ problem, in  
399 addition to regime-dependent (Table 2) and as in Xie and Zhang (2015),  $E_{auto}$  and  $E_{accr}$  should  
400 be also scale-dependent.

401 Also note that the location we choose to collect ground-based observations and retrievals is  
402 on the remote ocean where the MBL clouds mainly form in a relatively stable boundary layer  
403 and are characterized by high precipitation frequency. Even in such environments, however,  
404 the GCMs overestimate the precipitation frequency (Ahlgren and Forbes, 2014).

405 To further investigate how enhancement factors affect precipitation simulations, we use  
406  $E_{auto}$  as a fixed value of 3.2 in Eq. (4), and then calculate the  $q_c$  needed for models to reach the  
407 same autoconversion rate as observations. The  $q_c$  differences between models and observations  
408 are representing the amount of  $q_c$  needed for models to adjust to get a realistic autoconversion  
409 rate in the simulations. Similar to Figure 1, the PDFs of  $q_c$  differences (model – observation)  
410 are plotted in Figures 5a and 5b for 60-km and 180-km grid sizes. Figure 5c shows the average

411 percentages of model  $q_c$  adjustments for different model grid sizes. The mode and average  
412 values for 30-km grid is negative, suggesting that models need to simulate lower  $q_c$  in general  
413 to get reasonable autoconversion rates. Lower  $q_c$  values are usually associated with smaller  
414  $E_{auto}$  values that induce lower simulated precipitation frequency. On average, the percentage of  
415  $q_c$  adjustments decrease with increasing model grid size. For example, the adjustments for finer  
416 resolutions (e.g., 30-60 km) can be ~20% of the  $q_c$ , whereas adjustments in coarse resolution  
417 models (e.g., 120 – 180 km) are relatively small because the prescribed  $E_{auto}$  (=3.2) is close to  
418 the observed ones (Figure 4) and when model grid size is 180-km, no adjustment is needed.  
419 The adjustment method presented in Figure 5, however, may change cloud water substantially  
420 and may cause variety of subsequent issues, such as altering cloud radiative effects and  
421 disrupting the hydrological cycle. The assessment in Figure 5 only provides a reference to the  
422 equivalent effect on cloud water by using the prescribed  $E_{auto}$  value as compared to those from  
423 observations.

424 All above discussions are based on the prescribed  $E_{auto}$  and  $E_{accr}$  values (3.2 and 1.07) in  
425 MG08. Whereas there are quite a few parameterizations that have been published so far. In this  
426 study, we list  $E_{auto}$  and  $E_{accr}$  for three other widely used parameterization schemes in Table 3,  
427 which are given only for 60-km and 180-km grid sizes. The values of the exponent in each  
428 scheme directly affect the values of the enhancement factors. For example, the scheme in  
429 Beheng (1994) has highest degree of nonlinearity and hence has the largest enhancement

430 factors. The scheme in Liu and Daum (2004) is very similar to the scheme in Khairoutdinov  
431 and Kogan (2000) because both schemes have a physically realistic dependence on cloud water  
432 content and number concentration (Wood, 2005b). For a detailed overview and discussion of  
433 various existing parameterizations, please refer to Liu and Daum (2004), Liu et al. (2006a), Liu  
434 et al. (2004b) and Wood (2005b).

435

## 436 **5. Summary**

437 To better understand the influence of sub-grid cloud variations on the warm-rain process  
438 simulations in GCMs, we investigated the warm-rain parameterizations of autoconversion  
439 ( $E_{auto}$ ) and accretion ( $E_{accr}$ ) enhancement factors in MG08. These two factors represent the  
440 effects of sub-grid cloud and precipitation variabilities when parameterizing autoconversion  
441 and accretion rates as functions of grid-mean quantities.  $E_{auto}$  and  $E_{accr}$  are prescribed as 3.2  
442 and 1.07, respectively, in the widely used MG08 scheme. To assess the dependence of the two  
443 parameters on sub-grid scale variabilities, we used ground-based observations and retrievals  
444 collected at the DOE ARM Azores site to reconstruct the two enhancement factors in different  
445 model grid sizes.

446 From the retrieved  $q_c$  and  $q_r$  profiles, the averaged  $q_c$  within the top five range gates are  
447 used to calculate  $E_{auto}$  and the averaged  $q_c$  and  $q_r$  within five range gates around maximum  
448 reflectivity are used to calculate  $E_{accr}$ . The calculated  $E_{auto}$  values from observations and

449 retrievals increase from 1.96 at a grid box of 30×30 km to 3.15 at a grid box of 120×120 km.  
450 These values are 38% and 2% lower than the prescribed value of 3.2. The prescribed value in  
451 MG08 represents well in large grid sizes in GCMs. On the other hand, the  $E_{accr}$  values increase  
452 from 1.53 at a grid box of 30×30 km to 1.76 at a grid box of 180×180 km, which are 43% and  
453 64% higher than the prescribed value (1.07). The higher  $E_{auto}$  and lower  $E_{accr}$  prescribed in  
454 GCMs help to explain the issue of too frequent precipitation events with too light precipitation  
455 intensity. The ratios of rain to cloud liquid water increase with increasing  $E_{accr}$  from 0 to 2, and  
456 then decrease after that, suggesting a possible optimal state for the collision-coalescence  
457 process to achieve maximum efficiency for converting cloud water into rain water at  $E_{accr}=2$ .  
458 The ratios of  $q_r$  to  $q_c$  at  $E_{accr}=1.07$  and  $E_{accr}=2.0$  are 0.063 and 0.142, further proving that the  
459 prescribed value of  $E_{accr}=1.07$  is too small to simulate correct precipitation intensity in models.

460 To further investigate what conditions and parameters can significantly influence the  
461 enhancement factors, we classified low-level clouds according to their boundary layer  
462 conditions and CLWPs. Both  $E_{auto}$  and  $E_{accr}$  increase when the boundary layer conditions  
463 become less stable, and the values are larger in precipitating clouds ( $CLWP>75 \text{ gm}^{-2}$ ) than  
464 those in nonprecipitating clouds ( $CLWP<75 \text{ gm}^{-2}$ ). The  $E_{auto}$  values in both stable and mid-stable  
465 boundary layer conditions are smaller than the prescribed value of 3.2, while those in unstable  
466 boundary layers conditions are significantly larger than 3.2 regardless of whether or not the  
467 cloud is precipitating (Table 2). All  $E_{accr}$  values are greater than the prescribed value of 1.07.

468 Therefore, the selection of  $E_{auto}$  and  $E_{accr}$  values in GCMs should be regime-dependent, which  
469 also has been suggested by Hill et al. (2015) and Walters et al. (2017).

470 This study, however, did not include the effect of uncertainties in GCM simulated cloud  
471 and precipitation properties on sub-grid scale variations. For example, we did not consider the  
472 behavior of the two enhancement factors under different aerosol regimes, a condition which  
473 may affect precipitation formation process. The effect of aerosol-cloud-precipitation-  
474 interactions on cloud and precipitation sub-grid variabilities may be of comparable importance  
475 to meteorological regimes and precipitation status and deserves a further study. In addition,  
476 other factors may also affect precipitation frequency and intensity even under the same aerosol  
477 regimes and even if the clouds have similar cloud water contents. Wind shear, for example as  
478 presented in Wu et al. (2017), is an external variable that can affect precipitation formation.  
479 Further studies are needed to evaluate the role of the covariance of  $q_c$  and  $N_c$  in sub-grid scales  
480 on  $E_{auto}$  determinations, which is beyond the scope of this study and requires independent  
481 retrieval techniques.

482

### 483 **Appendix A: Joint cloud and rain LWC profile estimation**

484 If a time step is identified as non-precipitating, the cloud liquid water content (CLWC)  
485 profile is retrieved using Frisch et al. (1995) and Dong et al. (1998, 2014a and 2014b). The  
486 retrieved CLWC is proportional to radar reflectivity.

487 If a time step is identified as precipitating (maximum reflectivity below cloud base  
 488 exceeds -37 dBZ), CLWC profile is first inferred from temperature and pressure in merged  
 489 sounding by assuming adiabatic growth. Marine stratocumulus is close to adiabatic (Albrecht  
 490 et al. 1990) and was used in cloud property retrievals in literature (e.g., Rémillard et al., 2013).  
 491 In this study, we use the information from rain properties near cloud base to further constrain  
 492 the adiabatic CLWC ( $CLWC_{adiabatic}$ ).

493 Adopting the method of O'Connor et al. (2005), Wu et al. (2015) retrieved rain properties  
 494 below cloud base (CB) for the same period as in this study. In Wu et al. (2015), rain drop size  
 495 (median diameter,  $D_0$ ), shape parameter ( $\mu$ ), and normalized rain droplet number concentration  
 496 ( $N_W$ ) are retrieved for the assumed rain particle size distribution (PSD):

$$497 \quad n_r(D) = N_W f(\mu) \left(\frac{D}{D_0}\right)^\mu \exp\left[-\frac{(3.67+\mu)D}{D_0}\right] \quad (A1)$$

498 To infer rain properties above cloud base, we adopt the assumption in Fielding et al. (2015)  
 499 that  $N_W$  increases from below CB to within the cloud. This assumption is consistent with the *in*  
 500 *situ* measurement in Wood (2005a). Similar as Fielding et al. (2015), we use constant  $N_W$  within  
 501 cloud if the  $N_W$  decrease with height below CB. The  $\mu$  within cloud is treated as constant and  
 502 is taken as the averaged value from four range gates below CB. Another assumption in the  
 503 retrieval is that the evaporation of rain drops is negligible from one range gate above CB to one  
 504 range gate below CB thus we assume rain drop size is the same at the range gate below and  
 505 above CB.

506 With the above information, we can calculate the reflectivity contributed by rain at the first  
 507 range gate above CB ( $Z_d(1)$ ) and the cloud reflectivity ( $Z_c(1)$ ) is then  $Z_c(1) = Z(1) - Z_d(1)$ ,  
 508 where  $Z(1)$  is WACR measured reflectivity at first range gate above CB. Using cloud droplet  
 509 number concentration ( $N_c$ ) from Dong et al. (2014a and 2014b), CLWC at the first range gate  
 510 above CB can be calculated through

$$511 \quad Z_c(1) = 2^6 \int_0^\infty n_c(r) r^6 dr = \frac{36}{\pi^2 \rho_w^2} \frac{CLWC(1)_{reflectivity}^2}{N_c} \exp(9\sigma_x^2) \quad (A2)$$

512 where  $n_c(r)$  is lognormal distribution of cloud PSD with logarithmic width  $\sigma_x$  which is set to  
 513 a constant value of 0.38 (Miles et al., 2000),  $\rho_w$  is liquid water density.

514 We then compare the  $CLWC_{adiabatic}$  and the one calculated from  $CLWC_{reflectivity}$  at the  
 515 first range gate above CB. A scale parameter ( $s$ ) is defined as  $s = \frac{CLWC_{reflectivity}(1)}{CLWC_{adiabatic}(1)}$  and the  
 516 entire profile of  $CLWC_{adiabatic}$  is multiplied by  $s$  to correct the bias from cloud sub-  
 517 adiabaticity. Reflectivity profile from cloud is then calculated from Eq. (A2) and the remaining  
 518 reflectivity profile from WACR observation is regarded as rain contribution. Rain particle size  
 519 can then be calculated given that  $N_w$  and  $\mu$  are known and rain liquid water content (RLWC)  
 520 can be estimated.

521 There are two constrains used in the retrieval. One is that the summation of cloud and rain  
 522 liquid water path (CLWP and RLWP) must be equal to the LWP from microwave radiometer  
 523 observation. Another is that rain drop size ( $D_0$ ) near cloud top must be equal or greater than 50

524  $\mu m$  and if  $D_0$  is less than  $50 \mu m$ , we decrease  $N_W$  for the entire rain profile within cloud and  
525 repeat the calculation until the  $50 \mu m$  criteria is satisfied.

526 It is difficult to quantitatively estimate the retrieval uncertainties without aircraft in situ  
527 measurements. For the proposed retrieval method, 18% should be used as uncertainty for  
528 RLWC from rain properties in Wu et al. (2015) and 30% for CLWC from cloud properties in  
529 Dong et al. (2014a and 2014b). The actual uncertainty depends on the accuracy of merged  
530 sounding data, the detectability of WACR near cloud base and the effect of entrainment on  
531 cloud adiabaticity during precipitating. In the recent aircraft field campaign, the Aerosol and  
532 Cloud Experiments in Eastern North Atlantic (ACE-ENA) was conducted during 2017-2018  
533 with a total of 39 flights over the Azores, near the ARM ENA site on Graciosa Island. These  
534 aircraft in situ measurements will be used to validate the ground-based retrievals and  
535 quantitatively estimate their uncertainties in the future.

536 Figure A1 shows an example of the retrieval results. The merged sounding, ceilometer,  
537 microwave radiometer, WACR and ceilometer are used in the retrieval. Whenever one or more  
538 instruments are not reliable, that time step is skipped, and this results in the gaps in the CLWC  
539 and RLWC as shown in Figures A1(b) and A1(c). When the cloud is classified as  
540 nonprecipitating, no RLWC will be retrieved as well. Using air density ( $\rho_{air}$ ) profiles  
541 calculated from temperature and pressure in merged sounding, mixing ratio ( $q$ ) can be  
542 calculated from LWC using  $q(z) = LWC(z)/\rho_{air}(z)$ .

543 **Acknowledgements**

544 The ground-based measurements were obtained from the Atmospheric Radiation Measurement  
545 (ARM) Program sponsored by the U.S. Department of Energy (DOE) Office of Energy  
546 Research, Office of Health and Environmental Research, and Environmental Sciences  
547 Division. The data can be downloaded from <http://www.archive.arm.gov/>. This research was  
548 supported by the DOE CESM project under grant DE-SC0014641 at the University of Arizona  
549 through subaward from University of Maryland at Baltimore County, and the NSF project  
550 under grant AGS-1700728 at University of Arizona. The authors thank Dr. Yangang Liu at  
551 Brookhaven National Laboratory for insightful comments and Ms. Casey E. Oswant at the  
552 University of Arizona for proof reading the manuscript. The two anonymous reviewers are  
553 acknowledged for constructive comments and suggestions which helped to improve the  
554 manuscript.

555

556 **References**

557 Ackerman, A. S., Kirkpatrick, M. P., Stevens, D. E., and Toon, O. B.: The impact of humidity  
558 above stratiform clouds on indirect aerosol climate forcing, *Nature*, 432, 1014–1017, 2004.  
559 Ahlgrim, M., and Forbes, R.: Improving the Representation of Low Clouds and Drizzle in  
560 the ECMWF Model Based on ARM Observations from the Azores, *J. Clim.*, doi:  
561 10.1175/MWR-D-13-00153.1, 2014.  
562 Albrecht, B. A.: Aerosols, cloud microphysics, and fractional cloudiness, *Science*, 245, 1227–  
563 1231, 1989.

564 Albrecht, B., Fairall, C., Thomson, D., White, A., Snider, J., and Schubert, W.: Surface-based  
565 remote-sensing of the observed and the adiabatic liquid water-content of stratocumulus  
566 clouds, *Geophys. Res. Lett.*, 17, 89–92, doi:10.1029/G1017i001p00089, 1990.

567 Austin, P., Wang, Y., Kujala, V., and Pincus, R.: Precipitation in Stratocumulus Clouds:  
568 Observational and Modeling Results, *J. Atmos. Sci.*, 52, 2329–2352, doi:10.1175/1520-  
569 0469(1995)052<2329:PISCOA>2.0.CO;2, 1995.

570 Bai, H., Gong, C., Wang, M., Zhang, Z., and L'Ecuyer, T.: Estimating precipitation  
571 susceptibility in warm marine clouds using multi-sensor aerosol and cloud products from  
572 A-Train satellites, *Atmos. Chem. Phys.*, 18, 1763-1783, [https://doi.org/10.5194/acp-18-](https://doi.org/10.5194/acp-18-1763-2018)  
573 1763-2018, 2018.

574 Barker H. W., Wiellicki B.A., Parker L.: A parameterization for computing grid-averaged solar  
575 fluxes for inhomogeneous marine boundary layer clouds. Part II: Validation using satellite  
576 data. *J. Atmos. Sci.* 53: 2304–2316, 1996.

577 Beheng, K. D.: A parameterization of warm cloud microphysical conversion processes, *Atmos.*  
578 *Res.*, 33, 193-206, 1994.

579 Bony, S., and Dufresne, J.-L.: Marine boundary layer clouds at the heart of tropical cloud  
580 feedback uncertainties in climate models, *Geophys. Res. Lett.*, 32, L20806,  
581 doi:10.1029/2005GL023851, 2005.

582 Boutle, I. A., Abel, S. J., Hill, P. G., and Morcrette, C. J.: Spatial variability of liquid cloud and  
583 rain: Observations and microphysical effects. *Quart. J. Roy. Meteor. Soc.*, 140, 583–594,  
584 doi:10.1002/qj.2140, 2014.

585 Chen, T., Rossow, W. B., and Zhang, Y.: Radiative Effects of Cloud-Type Variations, *J. Clim.*,  
586 13, 264–286, 2000.

587 Cheng, A., and Xu. K.-M.: A PDF-based microphysics parameterization for simulation of  
588 drizzling boundary layer clouds, *J. Atmos. Sci.*, 66, 2317–2334,  
589 doi:10.1175/2009JAS2944.1, 2009.

590 Dong X., Ackerman, T. P., and Clothiaux, E. E.: Parameterizations of Microphysical and  
591 Radiative Properties of Boundary Layer Stratus from Ground-based measurements, *J.*  
592 *Geophys. Res.*, 102, 31,681-31,393, 1998.

593 Dong, X., Minnis, P., Ackerman, T. P., Clothiaux, E. E., Mace, G. G., Long, C. N., and  
594 Liljegren, J. C.: A 25-month database of stratus cloud properties generated from ground-  
595 based measurements at the ARM SGP site, *J. Geophys. Res.*, 105, 4529-4538, 2000.

596 Dong, X., Xi, B., Kennedy, A., Minnis, P. and Wood, R.: A 19-month Marine Aerosol-  
597 Cloud\_Radiation Properties derived from DOE ARM AMF deployment at the Azores:  
598 Part I: Cloud Fraction and Single-layered MBL cloud Properties, *J. Clim.*, 27,  
599 doi:10.1175/JCLI-D-13-00553.1, 2014a.

600 Dong, X., Xi, B., and Wu, P.: Investigation of Diurnal Variation of MBL Cloud Microphysical  
601 Properties at the Azores, *J. Clim.*, 27, 8827-8835, 2014b.

602 Fielding, M. D., Chiu, J. C., Hogan, R. J., Feingold, G., Eloranta, E., O'Connor, E. J. and  
603 Cadeddu, M. P.: Joint retrievals of cloud and drizzle in marine boundary layer clouds using  
604 ground-based radar, lidar and zenith radiances. *Atmospheric Measurement Techniques*, 8,  
605 pp. 2663-2683. ISSN 1867-8548 doi: 10.5194/amt-8-2663-2015, 2015.

606 Frisch, A., Fairall, C., and Snider, J.: Measurement of stratus cloud and drizzle parameters in  
607 ASTEX with a Ka-band Doppler radar and a microwave radiometer, *J. Atmos. Sci.*, 52,  
608 2788–2799, 1995.

609 Hahn, C. and Warren, S.: A gridded climatology of clouds over land (1971–96) and ocean  
610 (1954–97) from surface observations worldwide, Numeric Data Package NDP-026E  
611 ORNL/CDIAC-153, CDIAC, Department of Energy, Oak Ridge, Tennessee, 2007.

612 Hartmann, D. L., Ockert-Bell, M. E., and Michelsen, M. L.: The Effect of Cloud Type on  
613 Earth's Energy Balance: Global Analysis, *J. Climate*, 5, 1281–1304,  
614 [https://doi.org/10.1175/15200442\(1992\)005<1281:TEOCTO>2.0.CO;2](https://doi.org/10.1175/15200442(1992)005<1281:TEOCTO>2.0.CO;2), 1992.

615 Hartmann, D. L. and Short, D. A.: On the use of earth radiation budget statistics for studies of  
616 clouds and climate, *J. Atmos. Sci.*, 37, 1233–1250, doi:10.1175/1520-  
617 0469(1980)037<1233:OTUOER>2.0.CO;2, 1980.

618 Hill, P. G., Morcrette, C. J., and Boutle, I. A.: A regime-dependent parametrization of subgrid-  
619 scale cloud water content variability, *Q. J. R. Meteorol. Soc.*, 141, 1975–1986, 2015.

620 Houghton, J. T., Ding, Y., Griggs, D.J., Noguer, M., van der Linden, P.J., Dai, X., Maskell, K.,  
621 and Johnson, C.A.: *Climate Change: The Scientific Basis*, Cambridge University Press,  
622 881 pp, 2001.

623 Jess, S.: Impact of subgrid variability on large-scale precipitation formation in the climate  
624 model ECHAM5, PhD thesis, Dep. of Environ. Syst. Sci., ETH Zurich, Zurich,  
625 Switzerland, 2010.

626 Jiang, J., Su, H., Zhai, C., Perun, V. S., Del Genio, A., Nazarenko, L. S., Donner, L. J.,  
627 Horowitz, Seman, L., Cole, C., J., Gettelman, A., Ringer, M. A., Rotstayn, L., Jeffrey, S.,  
628 Wu, T., Brient, F., Dufresne, J-L., Kawai, H., Koshiro, T., Watanabe, M., LÉcuyer, T. S.,  
629 Volodin, E. M., Iversen, Drange, T., H., Mesquita, M. D. S., Read, W. G., Waters, J. W.,  
630 Tian, B., Teixeira, J., and Stephens, G. L.: Evaluation of cloud and water vapor simulations  
631 in CMIP5 climate models using NASA ‘‘A-train’’ satellite observations, *J. Geophys. Res.*,  
632 117, D14105, doi:10.1029/2011JD017237, 2012.

633 Kessler, E.: On the distribution and continuity of water substance in atmospheric circulations,  
634 *Met. Monograph* 10, No. 32, American Meteorological Society, Boston, USA, 84 pp.,  
635 1969.

636 Khairoutdinov, M. and Kogan, Y.: A New Cloud Physics Parameterization in a Large-Eddy  
637 Simulation Model of Marine Stratocumulus, *Mon. Wea. Rev.*, 128, 229-243, 2000.

638 Kooperman, G. J., Pritchard, M. S., Ghan, S. J., Wang, M., Somerville, R. C., and Russell, L.  
639 M.: Constraining the influence of natural variability to improve estimates of global aerosol

640 indirect effects in a nudged version of the Community Atmosphere Model 5, *J. Geophys.*  
641 *Res.*, 117, D23204, <https://doi.org/10.1029/2012JD018588>, 2012.

642 Larson, V. E., Nielsen, B. J., Fan, J., and Ovchinnikov, M.: Parameterizing correlations  
643 between hydrometeor species in mixed-phase Arctic clouds, *J. Geophys. Res.*, 116,  
644 D00T02, doi:10.1029/2010JD015570, 2011.

645 Larson, V. E., and Griffin, B. M.: Analytic upscaling of a local microphysics scheme. Part I:  
646 Derivation. *Quart. J. Roy. Meteor. Soc.*, 139, 46–57, 2013.

647 Lebesock, M. D., Morrison, H., and Gettelman, A.: Microphysical implications of cloud-  
648 precipitation covariance derived from satellite remote sensing, *J. Geophys. Res.-Atmos.*,  
649 118, 6521–6533, <https://doi.org/10.1002/jgrd.50347>, 2013.

650 Leon, D. C., Wang, Z., and Liu, D.: Climatology of drizzle in marine boundary layer clouds  
651 based on 1 year of data from CloudSat and Cloud-Aerosol Lidar and Infrared Pathfinder  
652 Satellite Observations (CALIPSO), *J. Geophys. Res.*, 113, D00A14,  
653 doi:10.1029/2008JD009835, 2008.

654 Liljegren, J. C., Clothiaux, E. E., Mace, G. G., Kato, S., and Dong, X.: A new retrieval for  
655 cloud liquid water path using a ground-based microwave radiometer and measurements of  
656 cloud temperature, *J. Geophys. Res.*, 106, 14,485-14,500, 2001.

657 Liu, Y. and Daum, P. H.: Parameterization of the autoconversion process, Part I: Analytical  
658 formulation of the Kessler-type parameterizations, *J. Atmos. Sci.*, 61, 1539–1548, 2004.

659 Liu, Y., Daum, P. H., and McGraw, R.: Parameterization of the autoconversion process. Part  
660 II: Generalization of Sundqvist-type parameterizations, *J. Atmos. Sci.*, 63, 1103–1109,  
661 2006a.

662 Liu, Y., Daum, P. H., McGraw, R., Miller, M.: Generalized threshold function accounting for  
663 effect of relative dispersion on threshold behavior of autoconversion process. *Geophys.*  
664 *Res. Lett.*, 33, L11804, 2006b.

665 Lohmann, U. and Feichter, J.: Global indirect aerosol effects: a review, *Atmos. Chem. Phys.*,  
666 5, 715–737, doi:10.5194/acp-5-715-2005, 2005.

667 Miles, N. L., Verlinde, J., and Clothiaux, E. E.: Cloud-droplet size distributions in low-level  
668 stratiform clouds. *J. Atmos. Sci.*, 57, 295–311, doi:10.1175/1520-0469(2000)057,  
669 0295:CDS DIL.2.0.CO;2, 2000.

670 Morrison, H. and Gettelman, A.: A new two-moment bulk stratiform cloud microphysics  
671 scheme in the Community Atmosphere Model, version 3 (CAM3). Part I: Description and  
672 numerical tests, *J. Climate*, 21, 3642–3659, 2008.

673 Nam, C., and Quaas, J.: Evaluation of clouds and precipitation in the ECHAM5 general  
674 circulation model using CALIPSO and CloudSat satellite data, *J. Clim.*, 25, 4975–4992,  
675 doi:10.1175/JCLI-D-11-00347.1, 2012.

676 O’Connor, E. J., Hogan, R. J., and Illingworth, A. J.: Retrieving stratocumulus drizzle  
677 parameters using Doppler radar and lidar, *J. of Applied Meteorol.*, 44, 14-27, 2005.

678 Pincus, R., McFarlane, S. A., and Klein, S. A.: Albedo bias and the horizontal variability of  
679 clouds in subtropical marine boundary layers: Observations from ships and satellites, *J.*  
680 *Geophys. Res.*, 104, 6183–6191, doi:10.1029/1998JD200125, 1999.

681 Pincus, R., and Klein, S. A.: Unresolved spatial variability and microphysical process rates in  
682 large-scale models. *J. Geophys. Res.*, 105D, 27 059–27 065, 2000.

683 Quaas, J., Ming, Y., Menon, S., Takemura, T., Wang, M., Penner, J. E., Gettelman, A.,  
684 Lohmann, U., Bellouin, N., Boucher, O., Sayer, A. M., Thomas, G. E., McComiskey, A.,  
685 Feingold, G., Hoose, C., Kristjánsson, J. E., Liu, X., Balkanski, Y., Donner, L. J., Ginoux,  
686 P. A., Stier, P., Grandey, B., Feichter, J., Sednev, Bauer, S. E., Koch, D., Grainger, R. G.,  
687 Kirkevåg, A., Iversen, T., Seland, Ø., Easter, R., Ghan, S. J., Rasch, P. J., Morrison, H.,  
688 Lamarque, J.-F., Iacono, M. J., Kinne, S., and Schulz, M.: Aerosol indirect effects –  
689 general circulation model intercomparison and evaluation with satellite data, *Atmos.*  
690 *Chem. Phys.*, 9, 8697–8717, <https://doi.org/10.5194/acp-9-8697-2009>, 2009.

691 Randall, D. A., Coakley, J. A., Fairall, C. W., Knopfli, R. A., and Lenschow, D. H.: Outlook  
692 for research on marine subtropical stratocumulus clouds. *Bull. Amer. Meteor. Soc.*, 65,  
693 1290–1301, 1984.

694 Rémillard, J., Kollias, P., Luke, E., and Wood, R.: Marine Boundary Layer Cloud Observations  
695 in the Azores, *J. Climate*, 25, 7381–7398, doi: [http://dx.doi.org/10.1175/JCLI-D-11-](http://dx.doi.org/10.1175/JCLI-D-11-00610.1)  
696 00610.1, 2012.

697 Rémillard, J., Kollias, P., and Szyrmer, W.: Radar-radiometer re- trievals of cloud number  
698 concentration and dispersion parameter in nondrizzling marine stratocumulus, *Atmos.*  
699 *Meas. Tech.*, 6, 1817–1828, doi:10.5194/amt-6-1817-2013, 2013.

700 Slingo, A.: Sensitivity of the Earth’s radiation budget to changes in low clouds, *Nature*, 343,  
701 49–51, <https://doi.org/10.1038/343049a0>, 1990.

702 Song, H., Zhang, Z., Ma, P.-L., Ghan, S. J., and Wang, M.: An Evaluation of Marine Boundary  
703 Layer Cloud Property Simulations in the Community Atmosphere Model Using Satellite  
704 Observations: Conventional Subgrid Parameterization versus CLUBB, *J. Clim.*,  
705 doi:10.1175/JCLI-D-17-0277.1, 2018.

706 Stanfield, R., Dong, X., Xi, B., Gel Genio, A., Minnis, P., and Jiang, J.: Assessment of NASA  
707 GISS CMIP5 and post CMIP5 Simulated Clouds and TOA Radiation Budgets Using  
708 Satellite Observations: Part I: Cloud Fraction and Properties, *J. Clim.*, doi:10.1175/JCLI-  
709 D-13-00588.1, 2014.

710 Tripoli, G. J. and Cotton, W. R.: A numerical investigation of several factors contributing to  
711 the observed variable intensity of deep convection over South Florida., *J. Appl. Meteorol.*,  
712 19, 1037–1063, 1980.

713 Troyan, D.: Merged Sounding Value-Added Product, Tech. Rep., DOE/SC-ARM/TR-087,  
714 2012.

715 Walters, D., Baran, A., Boutle, I., Brooks, M., Earnshaw, P., Edwards, J., Furtado, K., Hill, P.,  
716 Lock, A., Manners, J., Morcrette, C., Mulcahy, J., Sanchez, C., Smith, C., Stratton, R.,

717 Tennant, W., Tomassini, L., van Weverberg, K., Vosper, S., Willett, M., Browse, J.,  
718 Bushell, A., Dalvi, M., Essery, R., Gedney, N., Hardiman, S., Johnson, B., Johnson, C.,  
719 Jones, A., Mann, G., Milton, S., Rumbold, H., Sellar, A., Ujiie, M., Whittall, M., Williams,  
720 K. and Zerroukat, M. The Met Office Unified Model Global Atmosphere 7.0/7.1 and  
721 JULES Global Land 7.0 configurations. *Geosci. Model Dev.*, doi:10.5194/gmd-2017-291,  
722 2017.

723 Wang, M., Ghan, S., Liu, X., L'Ecuyer, T. S., Zhang, K., Morrison, H., Ovchinnikov, M.,  
724 Easter, R., Marchand, R., Chand, D., Qian, Y., and Penner, J. E.: Constraining cloud  
725 lifetime effects of aerosols using A-Train satellite observations, *Geophys. Res. Lett.*, 39,  
726 L15709, <https://doi.org/10.1029/2012GL052204>, 2012.

727 Warren, S. G., Hahn, C. J., London, J., Chervin, R. M., and Jenne, R.: Global distribution of  
728 total cloud cover and cloud type amount over land, Tech. Rep. Tech. Note TN-317 STR,  
729 NCAR, 1986.

730 Warren, S. G., Hahn, C. J., London, J., Chervin, R. M., and Jenne, R.: Global distribution of  
731 total cloud cover and cloud type amount over land, Tech. Rep. Tech. Note TN-317 STR,  
732 NCAR, 1988.

733 Weber, T., and Quaas, J.: Incorporating the subgrid-scale variability of clouds in the  
734 autoconversion parameterization using a PDF-scheme, *J. Adv. Model. Earth Syst.*, 4,  
735 M11003, doi:10.1029/2012MS000156, 2012.

736 Wielicki, B. A., Cess, R. D., King, M. D., Randall, D. A., and Harrison, E. F.: Mission to planet  
737 Earth: Role of clouds and radiation in climate, *Bull. Amer. Meteor. Soc.*, 76, 2125–2153,  
738 doi:10.1175/1520-0477(1995)076<2125:MTPERO.2.0.CO;2, 1995.

739 Wood, R., Field, P. R., and Cotton, W. R.: Autoconversion rate bias in stratiform boundary  
740 layer cloud parameterization. *Atmos. Res.*, 65, 109–128, 2002.

741 Wood, R.: Drizzle in stratiform boundary layer clouds. Part I: Vertical and horizontal structure,  
742 *J. Atmos. Sci.*, 62, 3011–3033, 2005a.

743 Wood, R.: Drizzle in stratiform boundary layer clouds. Part II: Microphysical aspects, J.  
744 Atmos. Sci., 62, 3034–3050, 2005b.

745 Wood, R. and Hartmann, D.: Spatial variability of liquid water path in marine low cloud: The  
746 importance of mesoscale cellular convection, J. Climate, 19, 1748–1764, 2006.

747 Wood, R.: Cancellation of aerosol indirect effects in marine stratocumulus through cloud  
748 thinning. J. Atmos. Sci., 64, 2657–2669, 2007.

749 Wood, R.: Stratocumulus Clouds, Mon. Wea. Rev., 140, 2373–2423. doi:  
750 <http://dx.doi.org/10.1175/MWR-D-11-00121.1>, 2012.

751 Wood, R., Wyant, M., Bretherton, C. S., Rémillard, J., Kollias, P., Fletcher, J., Stemmler, J.,  
752 deSzoek, S., Yuter, S., Miller, M., Mechem, D., Tselioudis, G., Chiu, C., Mann, J.,  
753 O'Connor, E., Hogan, R., Dong, X., Miller, M., Ghate, V., Jefferson, A., Min, Q., Minnis,  
754 P., Palinkonda, R., Albrecht, B., Luke, E., Hannay, C., Lin, Y.: Clouds, Aerosol, and  
755 Precipitation in the Marine Boundary Layer: An ARM Mobile Facility Deployment, Bull.  
756 Amer. Meteorol. Soc., doi: <http://dx.doi.org/10.1175/BAMS-D-13-00180.1>, 2015.

757 Wu, P., Dong, X. and Xi, B.: Marine boundary layer drizzle properties and their impact on  
758 cloud property retrieval, Atmos. Meas. Tech., 8, 3555–3562. doi: 10.5194/amt-8-3555-  
759 2015, 2015.

760 Wu, P., Dong, X., Xi, B., Liu, Y., Thieman, M., and Minnis, P.: Effects of environment forcing  
761 on marine boundary layer cloud-drizzle processes, J. Geophys. Res. Atmos., 122, 4463–  
762 4478, doi:10.1002/2016JD026326, 2017.

763 Xie, X., and Zhang, M.: Scale-aware parameterization of liquid cloud inhomogeneity and its  
764 impact on simulated climate in CESM, J. Geophys. Res. Atmos., 120, 8359–8371,  
765 doi:10.1002/2015JD023565, 2015.

766 Yoo, H., and Li, Z.: Evaluation of cloud properties in the NOAA/NCEP Global Forecast  
767 System using multiple satellite products. Climate Dyn., 39, 2769–2787,  
768 doi:10.1007/s00382-012-1430-0, 2012.

769 Yoo, H., and Li, Z., Hou, Y.-T., Lord, S., Weng, F., and Barker, H. W.: Diagnosis and testing  
770 of low-level cloud parameterizations for the NCEP/GFS using satellite and ground-based  
771 measurements. *Climate Dyn.*, 41, 1595–1613, doi:10.1007/s00382-013-1884-8, 2013.

772 Zhang, J., Lohmann, U., and Lin, B.: A new statistically based autoconversion rate  
773 parameterization for use in large-scale models. *J. Geophys. Res.*, 107, 4750,  
774 doi:10.1029/2001JD001484, 2002.

775 Zhang, Z., Song, H., Ma, P.-L., Larson, V., Wang, M., Dong, X., and Wang, J.: Subgrid  
776 variations of cloud water and droplet number concentration over tropical oceans: satellite  
777 observations and implications for warm rain simulation in climate models. Submitted to  
778 *Atmos. Chem. Phys.*, 2018.

779

780 **Table 1. The parameters of autoconversion and accretion formulations for four**  
 781 **parameterizations.**

782

	<i>A</i>	<i>a1</i>	<i>a2</i>	<i>B</i>	<i>b</i>
Khairoutdinov and Kogan (2000)	1350	2.47	-1.79	67	1.15
	$1.3 \times 10\beta_6^6$ ,				
	where $\beta_6^6 = [(r_v + 3)/r_v]^2$ ,				
Liu and Daum (2004)	$r_v$ is mean volume radius.	3	-1	N/A	N/A
	modification was made by Wood (2005b)				
Tripoli and Cotton (1980)	3268	7/3	-1/3	1	1
Beheng (1994)	$3 \times 10^{34}$ for $N_c < 200 \text{ cm}^{-3}$ 9.9 for $N_c > 200 \text{ cm}^{-3}$	4.7	-3.3	1	1

783

784 **Table 2. Autoconversion (left) and accretion (right) enhancement factors in different**  
 785 **boundary layer conditions (LTS > 18 K for stable, LTS < 13.5 K for unstable and LTS**  
 786 **within 13.5 and 18 K for mid-stable) and in different LWP regimes (LWP ≤ 75 g m<sup>-2</sup> for**  
 787 **non-precipitating and LWP > 75 g m<sup>-2</sup> for precipitating).**  
 788

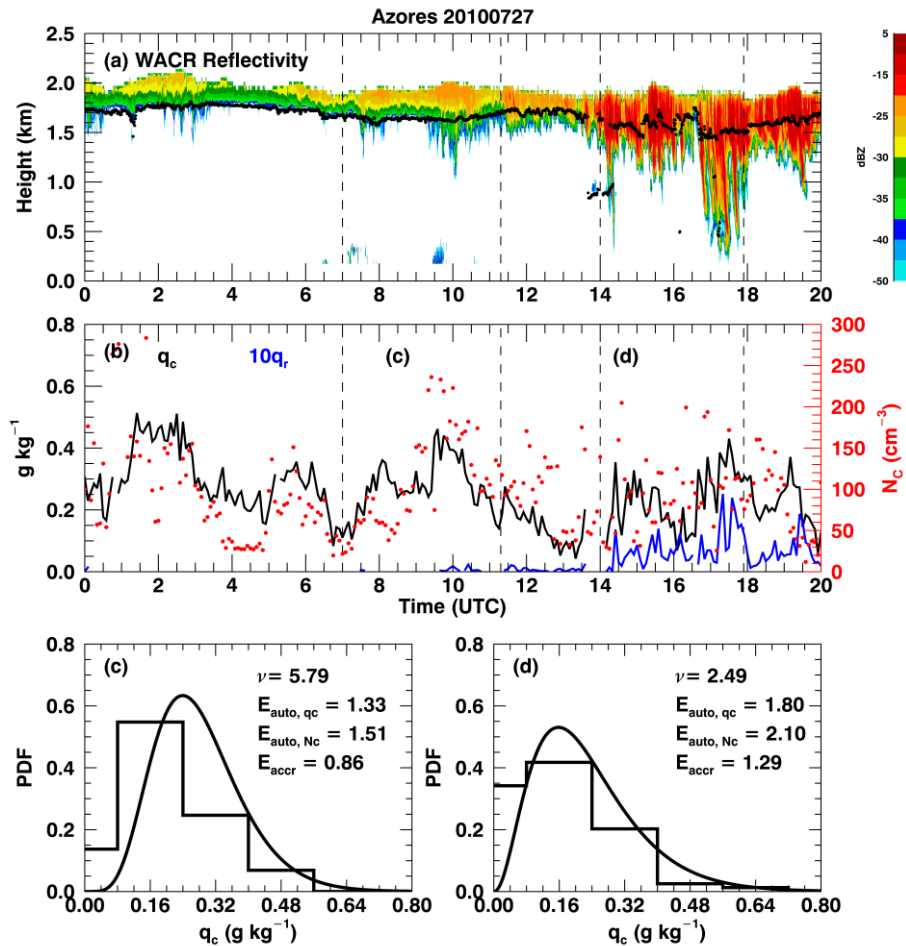
LTS (K)	LWP ≤ 75 g m <sup>-2</sup>	LWP > 75 g m <sup>-2</sup>
> 18	2.32/1.42	2.75/1.52
(13.5, 18)	2.61/1.47	3.07/1.68
< 13.5	4.62/1.72	6.94/1.86

789

790 **Table 3. Autoconversion and accretion enhancement factors ( $E_{auto}$  and  $E_{accr}$ ) for the**  
 791 **parameterizations in Table 1 except the Khairoutdinov and Kogan (2000) scheme. The**  
 792 **values are averaged for 60-km and 180-km model grids.**  
 793

	$E_{auto}$		$E_{accr}$	
	60-km	180-km	60-km	180-km
Liu and Daum (2004)	3.82	4.23	N/A	N/A
Tripoli and Cotton (1980)	2.46	2.69	1.47	1.56
Beheng (1994)	6.94	5.88	1.47	1.56

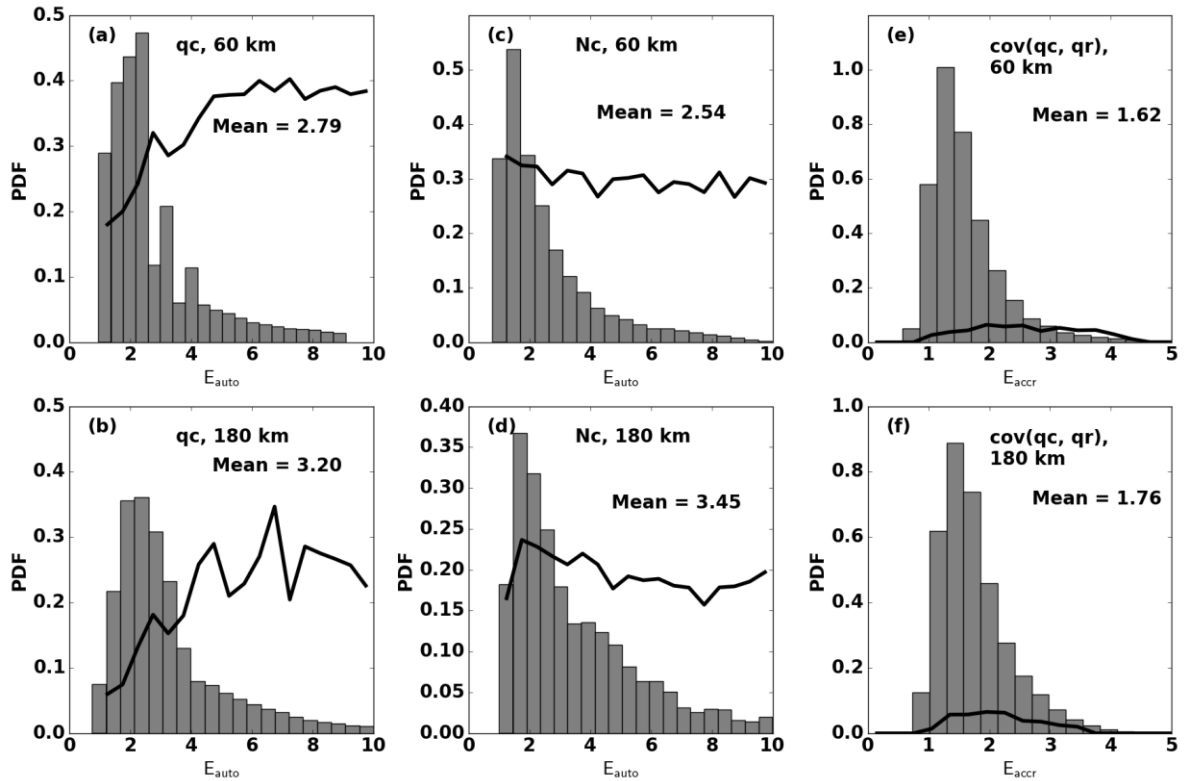
794



795

796 **Figure 1. Observations and retrievals over Azores on 27 July 2010. (a) W-band ARM**  
 797 **cloud radar (WACR) reflectivity (contour) superimposed with cloud-base height (black**  
 798 **dots). (b) Black line represents averaged cloud water mixing ratio ( $q_c$ ) within the top five**  
 799 **range gates, blue line represents averaged rain ( $\times 10$ ) water mixing ratio within five range**  
 800 **gates around maximum reflectivity, red dots are the retrieved cloud droplet number**  
 801 **concentration ( $N_c$ ). Dashed lines represent two periods that have 60 km model grids with**  
 802 **similar mean- $q_c$  but different distributions as shown by step lines in (c) and (d). Curved**  
 803 **lines in (c) and (d) are fitted gamma distributions with the corresponding shape**  
 804 **parameter ( $\nu$ ) shown on the upper right.  $N_c$  distributions are not shown. The calculated**  
 805 **autoconversion ( $E_{auto, q_c}$  from  $q_c$  and  $E_{auto, N_c}$  from  $N_c$ ) and accretion ( $E_{accr}$ )**  
 806 **enhancement factors are also shown.**

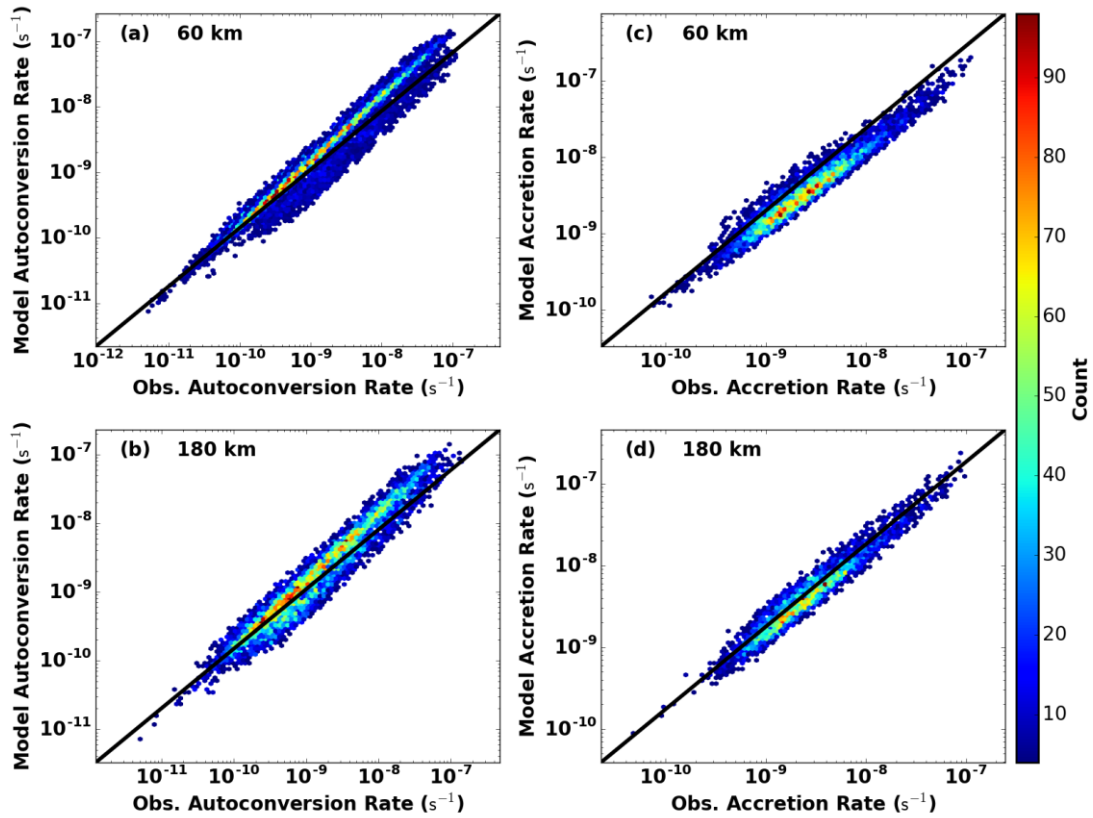
807  
808



809

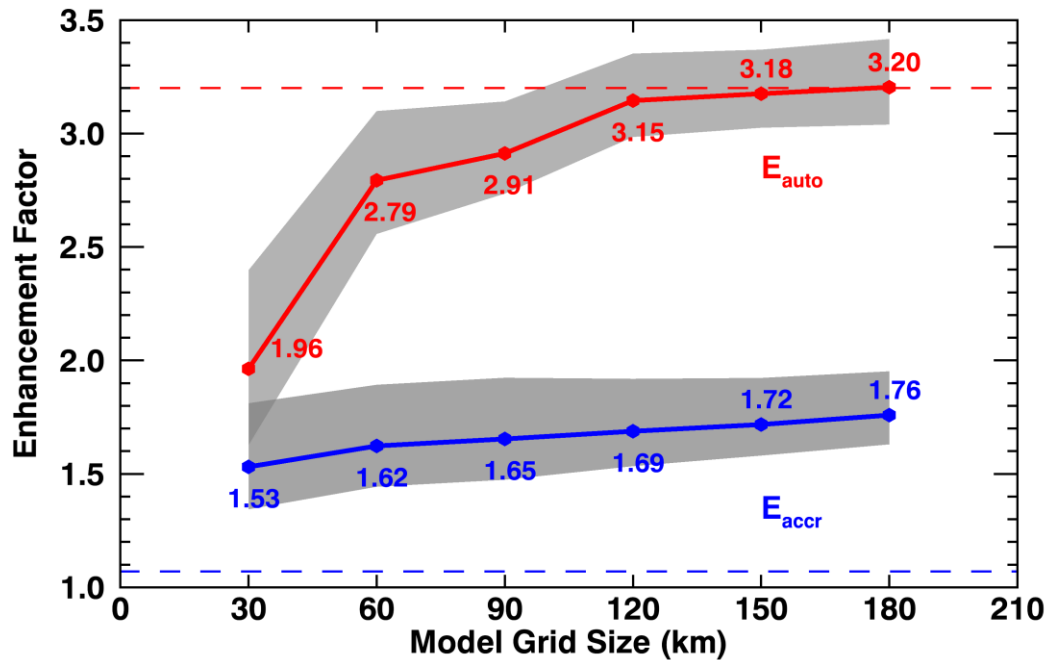
810 **Figure 2. Probability density functions (PDFs) of autoconversion (a - d) and accretion (e**  
811 **- f) enhancement factors calculated from  $q_c$  (a-b),  $N_c$  (c-d), and the covariance of  $q_c$  and**  
812  **$q_r$  (e-f). The two rows show the results from 60-km and 180-km model grids, respectively,**  
813 **with their average values. Black lines represent precipitation frequency in each bin in (a)-**  
814 **(d) and the ratio of layer-mean  $q_r$  to  $q_c$  in (e)-(f).**

815



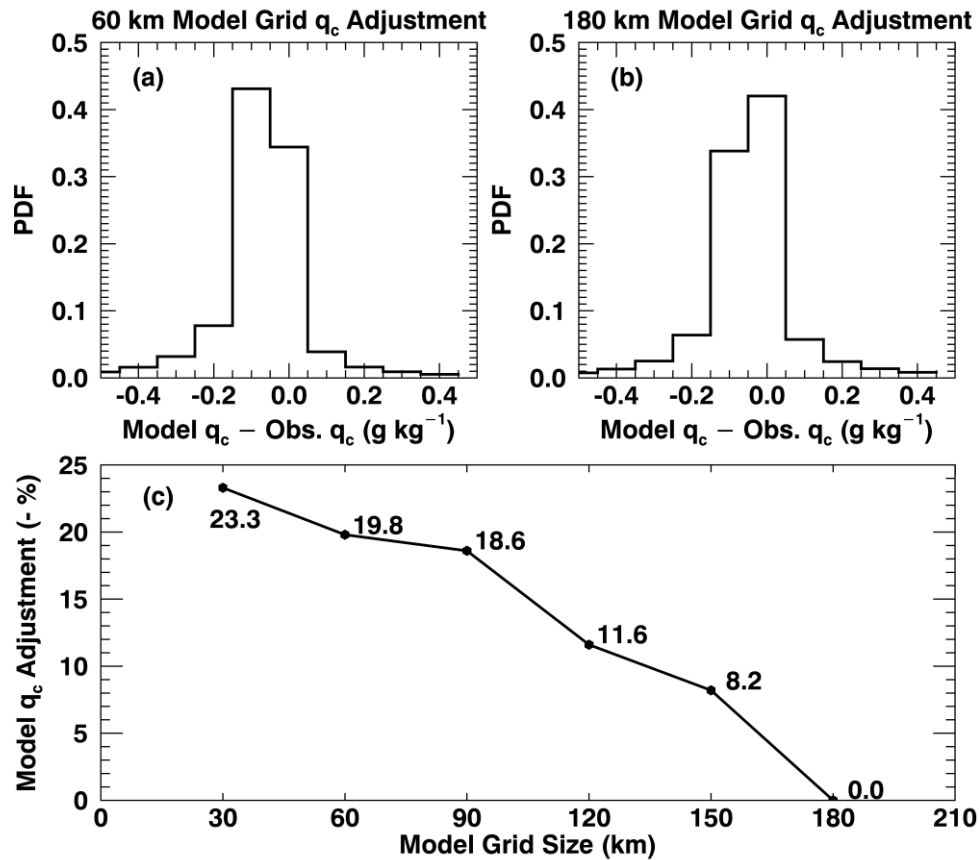
816

817 **Figure 3.** Comparison of autoconversion (a-b) and accretion (c-d) rates derived from  
 818 observations (x-axis) and from model (y-axis). Results are for 60-km (a and c) and 180-  
 819 km model grids. Colored dots represent joint number densities.



821 **Figure 4. Autoconversion (red line) and accretion (blue line) enhancement factors as a**  
 822 **function of model grid sizes. The shaded areas are calculated by varying  $q_c$  and  $q_r$  within**  
 823 **their retrieval uncertainties. The two dashed lines show the constant values of**  
 824 **autoconversion (3.2) and accretion (1.07) enhancement factors prescribed in MG08.**

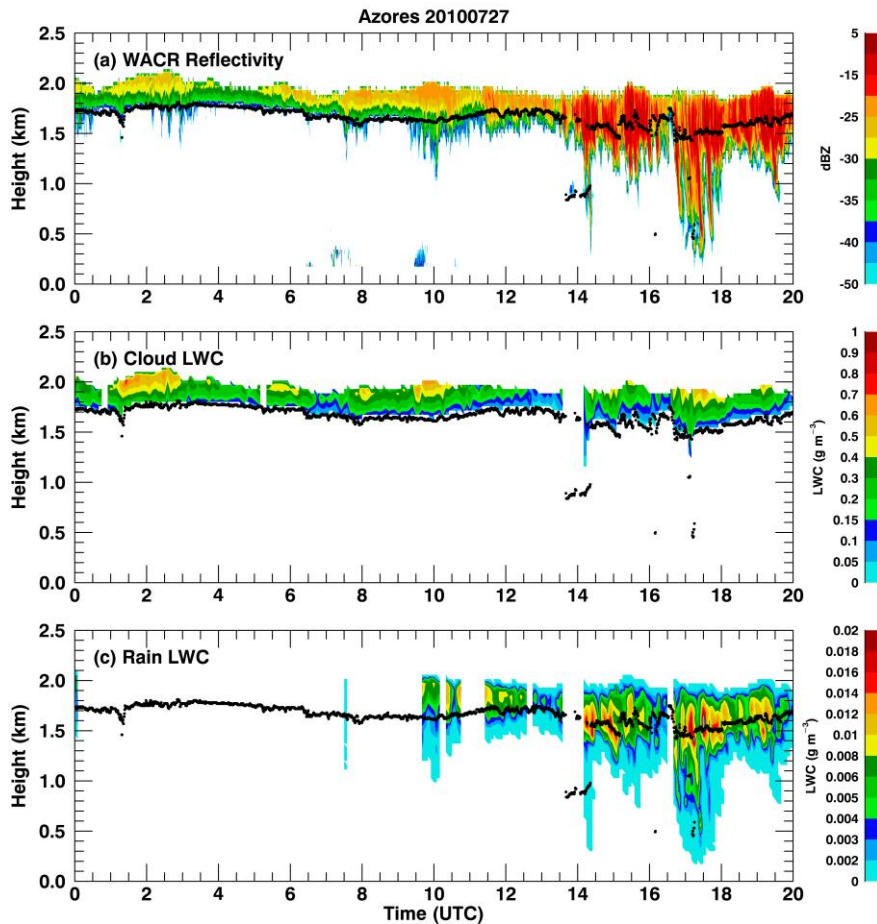
825



826

827 **Figure 5.**  $q_c$  needed for models to adjust to reach the same autoconversion rate as  
 828 **observations for (a) 60-km and (b) 180-km model grids. Positive biases represent**  
 829 **increased  $q_c$  are required in models and negative biases mean decreased  $q_c$ . The average**  
 830 **percentages of adjustments for different model grid sizes are shown in panel (c) and note**  
 831 **that the percentages in the vertical axis are negative.**

832



833

834 **Figure A1. Joint retrieval of cloud and rain liquid water content (CLWC and RLWC) for**  
 835 **the same case as in Figure 1. (a) WACR reflectivity, (b) CLWC, and (c) RLWC. The black**  
 836 **dots represent cloud base height. Blank gaps are due to the data from one or more**  
 837 **observations are not available or reliable. For example, the gap before 14 UTC is due to**  
 838 **multiple cloud layers are detected whereas we only focus on single layer cloud.**